AMS Home   Journals Home   Journal Archive   Subscribe   For Authors   Help   Advanced Search | Search | Go |

Full Text View

Reynolds Stresses and Secondary Circulation in a Stratified Rotating Shear Flow

Michael W. Ott[*], Richard Dewey, and Chris Garrett

Centre for Earth and Ocean Research, University of Victoria, Victoria, British Columbia, Canada

ABSTRACT

A transverse secondary circulation should result from vertical mixing of momentum in a stratified shear flow influenced by the earth's rotation. A rigidly mounted acoustic Doppler current profiler was deployed at the bottom of Juan de Fuca Strait, a stratified estuary on the west coast of North America, for 21 days, to examine this dynamical process and its variation over a spring–neap tidal cycle. The data demonstrate a significant fortnightly modulation of the estuarine exchange flow, with stronger along-channel flow, less dynamic stability, and much greater cross-strait currents at neap tide than at spring tide. Reliable estimates of the Reynolds stresses in the stratified shear flow away from boundaries were also obtained. They were small except for several days around neap tide when they were associated with times of reduced Richardson number. These stresses are not related in any simple way (such as with a smooth, positive, eddy viscosity) to the shear of the mean flow but do have a pattern of vertical divergence that is similar to that of the cross-strait flow. A limited time series of microstructure profiles also shows enhanced mixing during a period of large Reynolds stresses.

1. Introduction

The mean along-channel circulation in an estuary is often dominated by an outflow in the upper layer and deep inflow of saltier ocean water. The deep return flow is required to maintain the salt balance of the estuary as the outflow becomes brackish through entrainment of salt from below. The strength of the return flow depends on the amount of entrainment, that is, the rate of mixing, into the upper layer as it flows from the river mouth to the sea. This has been well studied for a variety of estuaries (e.g., Rattray and Hansen 1962; Fischer et al. 1979; Labrecque et al. 1994; Mertz and Gratton 1995).

The cross-channel flow has been examined much less extensively, despite its importance in dispersing scalars throughout an estuary system and in opposing the along-channel exchange by redistributing momentum. Cross-channel flow may be associated with curvature of the axis of an estuary but may also occur in straight channels as a consequence of internal friction and the earth's rotation, as found by Johnson and Ohlsen (1994) in laboratory experiments on rotating two-layer exchange. They found significant transverse circulation near the interface, consistent with internal Ekman layers caused by a frictionally induced breakdown of the geostrophic balance there (Csanady 1972).

The Johnson and Ohlsen (1994) experiments were for a two-layer situation, but transverse flows can also be expected for more continuous stratification if internal friction breaks the geostrophic balance. For example, Mertz and Gratton (1995) examined cross-channel flow in the Saint Lawrence River and found some evidence for ageostrophic transverse currents associated with a vertical eddy viscosity of about 0.004 $m^2 s^{-1}$. Ageostrophic transverse currents were also observed by Johnson and Sanford (1992) in regions of large vertical shear of the along-channel flow in the Faroe Channel, but these were based on only a few vertical profiles. The cross-channel currents were seen in both the bottom boundary layer and the interface between the lower dense outflow into the Atlantic Ocean and the water above.

In Juan de Fuca Strait, which is the setting of the present paper, Ott and Garrett (1998) used an along-channel momentum balance to estimate that the vertical eddy viscosity near the diffuse interface between outflow and inflow might be as large as about 0.02 $m^2 s^{-1}$ in May and perhaps even larger in summer because of the enhanced estuarine exchange resulting from the June freshet. This internal friction might result in cross-strait ageostrophic currents on the order of 0.01 $m s^{-1}$, in opposite directions on either side of the interface. Ott and Garrett (1998) did find cross-strait flows of this magnitude in historical rotary current meter data from May of 1973, but apparently in the same direction above and below the interfacial depth and with very poor vertical resolution.

Data with excellent vertical resolution can now be obtained from acoustic Doppler current profilers (ADCPs) and these can also provide estimates of the Reynolds stresses associated with the generation of ageostrophic transverse flows. Most successful measurements of Reynolds stresses to date have been in unstratified, or very weakly stratified, water and sufficiently close to the bottom that it was the primary source of the turbulence (Lohrmann et al. 1990; Lu and Lueck 1999; Stacey et al. 1999a,b), although R. F. Marsden and R. G. Ingram (2001, personal communication) recently found significant Reynolds stresses beneath the base of the mixed layer in the Arctic.

Given the importance of understanding internal mixing and secondary circulation in stratified shear flows in general, we have sought to exploit the fairly straight and smooth-sided Juan de Fuca Strait as a natural laboratory. Ott and Garrett's (1998) estimated vertical eddy viscosity of $A_v \simeq 0.02$ $m^2 s^{-1}$, combined with a vertical shear U_z for the along-strait current of about $3 \times 10^{-3} s^{-1}$ in May, implies a mean Reynolds stress of $-\overline{u'w'} = A_v U_z \approx 10^{-4}$ $m^2 s^{-2}$. Larger values might occur during periods of elevated turbulent or internal wave activity.

Stresses of these magnitudes should be measurable with acoustic techniques. This paper describes an observational program involving hydrography, a bottom-moored ADCP, and microstructure profiles carried out in Juan de Fuca Strait during the summer of 1996 that was designed to observe the expected mixing and stresses. After a brief description of Juan de Fuca Strait, the observations are presented, followed by analysis and discussion.

2. Juan de Fuca Strait

Juan de Fuca Strait (Fig. 1 ⬤) is a 120-km-long estuarine channel, approximately 20 km wide and 200 m deep in the central section. It is oriented in a WNW–ESE direction, is fairly straight, and has relatively smooth bathymetry. West of the entrance, Juan de Fuca Canyon, with a depth of over 300 m, cuts southwestward through the continental shelf. The eastern portion of Juan de Fuca Strait shallows to 100 m at a sill south of Victoria before breaking up into a number of smaller channels among the San Juan and Gulf Islands.

The strait is important and interesting in its own right, as a major recreation and fisheries region and as a shipping lane to Vancouver and Seattle. It is also a useful test basin in which to study the effects of mixing on a stratified rotating shear flow. As mentioned above, secondary circulations should be observable and Reynolds stresses and mixing rates should be large enough to be measured and compared with the subgrid-scale parameterizations used in numerical models.

Mixing in the strait is largely associated with the strong tidal currents, typically about 1 $m s^{-1}$. The stratification arises from the strait being the main outlet for the Strait of Georgia and Puget Sound basins, draining much of the precipitation falling over southern British Columbia and northern Washington State. The freshwater input into these basins has a large seasonal cycle, with a winter minimum of typically 5000 $m^3 s^{-1}$ and a summer maximum of 25 000 $m^3 s^{-1}$ during the freshet that results from snowmelt in the mountains. Fraser River discharge is the dominant buoyancy input during the

summer and accounts then for approximately 50% of the total freshwater forcing (Griffin and LeBlond 1990). As a consequence, the estuarine circulation in Juan de Fuca is seasonal, peaking in June and July.

Offshore winds are generally northward in winter; the southeastward winds of summer drive coastal upwelling along the western side of Vancouver Island and Washington State, bringing colder, saltier water from the deep Pacific up through the offshore canyon and into Juan de Fuca Strait. The combination of a saltier deep layer and the increased freshwater discharge in summer results in enhanced stratification. Partly because of these seasonal variations, there has been some debate historically as to whether the estuarine characteristics of Juan de Fuca Strait are better described as stratified or as well-mixed.

One parameter used to classify estuaries is the estuarine Richardson number, defined as

$$\text{Ri}_e = \frac{g\Delta\rho}{\rho_o}\frac{Q_f}{Wu_{\text{rms}}^3}, \qquad (1)$$

where g is gravitational acceleration, ρ_o is the average density of water in the strait, $\Delta\rho$ is the density difference from freshwater, Q_f is the freshwater influx, W is the channel width, and u_{rms} is the rms tidal velocity. It is a measure of the stabilizing influence of stratification versus the mixing power of the tidal currents. It can also be used as a guide to the diffusive fraction of the up-estuary salt flux. This fraction is zero in a perfect two-layer estuarine flow and increases continuously through the salt wedge and partially stratified cases to become unity for an estuary with vertically homogeneous density.

In winter, Ri_e for Juan de Fuca is approximately 0.5, within the transition region of 0.08–0.8 from well-mixed to strongly stratified (Fischer et al. 1979). In summer Ri_e is approximately 1, suggesting a more stratified environment.

Following the approach used by Hansen and Rattray (1966), however, MacCready (1999) showed that two nondimensional parameters are needed to classify an estuary. These can be the ratios of the tidal velocity and the river velocity (i.e., the freshwater input divided by the cross-sectional area) to the internal wave speed, and they are denoted by Γ and F_m. If lines of constant Ri_e are plotted on the (Γ, F_m) phase-space diagram of MacCready (1999), they do not coincide with the contours of constant diffusive fraction, implying that the estuarine Richardson number is not sufficient to adequately determine the estuary type. Nonetheless, MacCready (1999) found that Juan de Fuca Strait lies in the region of parameter space for which the up-estuary salt flux is dominated by the exchange flow; the diffusive fraction of the up-estuary salt flow is slightly greater than 0.1 in winter and is less than 0.1 in summer. In descriptive terms, Juan de Fuca Strait varies from a partially stratified estuary in the winter to a well-stratified estuary in the summer.

There are shorter-term variations in the nature of the strait, however. Buoyancy input into Juan de Fuca Strait is largest during neap tides, when vertical mixing in the islands to the east is reduced. Griffin and LeBlond (1990) state that this mixing region acts as a periodic barrier separating Juan de Fuca Strait from the Strait of Georgia, "because the vertical exchange of momentum (during spring tides) inhibits the sheared flow that would commence if mixing were to cease." The spring–neap variation is reduced in strength in autumn and spring because of the smaller solar declinational tide, so the greatest fluctuations of buoyancy input into Juan de Fuca Strait should occur in early summer. Using surface salinity records from between 1967 and 1985, Griffin and LeBlond (1990) show that salinity fluctuations at Race Rocks (in the eastern portion of Juan de Fuca; Fig. 1 ⬤) are indeed greatest during the summer months and that more than 47% of the salinity variance can be accounted for by the M_m (period 27.55 days) and MS_f (14.76 days) tidal components.

Masson and Cummins (2000) examined the effects of a spring–neap cycle in tidal mixing over the Victoria sill and in Haro Strait on the regional circulation. Although they did not explicitly include the tides, they modeled the tides' effects by varying the mixing coefficients over a fortnightly cycle. They were able to reproduce both the magnitude of the spring–neap variation in the surface salinity at Race Rocks, about 1 psu, and its phase relative to the tide, with lowest salinities occurring 2 days after neap tide. They suggested from their model results that the volume of the estuarine exchange flow across the central section of Juan de Fuca Strait is largest during the several days at neap tide and smallest during springs, with a fortnightly modulation of nearly 20% of the mean. The model results also suggest that mixing within Juan de Fuca Strait itself is larger during neap tide (P. Cummins 2000, personal communication), likely because of the larger shears associated with the increase in estuarine exchange. No inference was made regarding the likelihood that mixing within Juan de Fuca Strait may cause a secondary circulation near the interface.

3. Observations: 1996

An observational program in Juan de Fuca Strait was carried out from the MSV *Strickland,* the University of Victoria's

16-m research vessel, between July and August of 1996. Summer was chosen to coincide with the peak runoff of the Fraser River and hence seasonally maximum along-strait surface currents in Juan de Fuca Strait, in the expectation that cross-channel currents might also be largest then. Over the entire period, winds within the strait were very light, the sky was nearly cloudless, and swell entering Juan de Fuca Strait from the Pacific Ocean was low.

a. ADCP

A four-beam 300-kHz broadband ADCP was deployed on 17 July 1996 and was recovered on 7 August. It was bottom mounted in a gimballed bracket, allowing free pitch and roll movement to accommodate any bottom slope up to 15°. It was deployed at 130-m depth, approximately 7 km offshore from Jordan River atop a small submarine hill, with along- and cross-channel dimensions of 3 and 1 km, respectively, rising nearly 30 m from the surrounding region (Fig. 1 ⦿). This site was selected so that the 100-m range of the instrument would permit sampling at depths between about 30 and 120 m at a distance far enough from shore to avoid boundary interactions. The ADCP was programmed to record beam velocity ensembles every 30 s for 54 vertical bins of 2-m depth, where each ensemble consisted of 35 pings over 11 s (i.e., burst mode). Valid data were returned during the entire 21-day period.

The ADCP data return was, however, strongly influenced by vertically migrating zooplankton. At dawn, the zooplankton migrate to a depth of between 80 and 120 m to avoid predation, and at dusk they migrate to the surface to feed on phytoplankton. These migration patterns affected the acoustic signal returned to the ADCP. During the night, good-quality ADCP data were returned throughout the entire 110-m range; during the day, the upper 30 m was lost. As a consequence, for the majority of the analysis which follows we consider only the lower 80 m of the water column ADCP data, from the bottom to 50 m below the surface, where observations were continuous.

b. Hydrography

Daily surface salinities recorded at Race Rocks reveal that the surface water was anomalously fresh during the period of deployment of our bottom-mounted ADCP (Fig. 2 ⦿). These freshwater pulses are generally associated with northwest winds in the Strait of Georgia, which tend to divert the less-mixed freshet toward Juan de Fuca, especially during weaker neap tides (Griffin and LeBlond 1990). During such events, models predict that the estuarine exchange is enhanced beyond the increase normally associated with the spring–neap cycle (Masson and Cummins 2000).

Other hydrographic observations were made at sea in three stages: 16–19 July (during the ADCP deployment), 24–26 July, and 5–7 August (ADCP recovery). An Applied Microsystems STD-12+ was used on each of the three cruises to obtain 147 salinity and temperature profiles (Fig. 1 ⦿). The CTD sampling rate of 2 Hz limited vertical resolution to between 0.3 and 0.5 m for the 1 m s^{-1} descent rates used. This resolution was sufficient to determine the vertical gradient of the geostrophic velocity via the thermal wind equation.

One along-channel transect (consisting of eight midchannel stations beginning south of Victoria and ending north of Cape Flattery) and one cross-channel transect (10 stations between Jordan River, British Columbia, and Pillar Point, Washington) were obtained during each cruise (Fig. 1 ⦿). An additional cross-channel transect was made during the second cruise.

Along-channel transects from each of the cruises are qualitatively similar, revealing a shallowing of isopycnals in the seaward direction, as required to drive the lower return flow (Fig. 3a ⦿). A Coriolis-induced cross-channel isopycnal slope is also persistent, with a slope of about 2×10^{-3} (Fig. 3b ⦿) in the 26.0 kg m^{-3} isopycnal, which coincided with the level of average zero along-channel flow in the present data as well as in the 1973 current meter data examined by Ott and Garrett (1998).

During the second cruise, a CTD time series of 60 profiles over 9 h on 25 July was taken at the ADCP mooring (Fig. 3c ⦿). This series shows no obvious modulation with the tides, as represented by the tidal current at 80 m (Fig. 3d ⦿). There was a similar lack of variability in the density structure over the spring–neap cycle (not shown); the mean density profile and resulting buoyancy frequency are shown in Figs. 3e and 3f ⦿, respectively.

c. Microstructure

On 5 and 6 August 1996, a limited number of turbulent microstructure profiles were obtained using a free-fall vertical profiler (Dewey et al. 1987). The measurements consisted of fast- and slow-response temperature profiles and two components of microstructure velocity shear. The profiler descends at a rate of approximately 0.7–0.8 m s^{-1}, landing on the bottom in water less than 300 m deep. Turbulent dissipation rate estimates were calculated from 1024 point spectra of the microstructure shear following the method of Dewey and Crawford (1988). On 5 August, 37 profiles were collected near the ADCP mooring site during the transition from a flood tide to an ebb tide. On 6 August, a transect of 24 microstructure profiles was made across Juan de Fuca Strait. The time series of turbulent dissipation rates provides a brief independent

estimate of the timing and location of turbulent mixing throughout the water column.

4. Analysis

a. ADCP currents

Tides were extracted from the 21-day ADCP current meter records using a standard harmonic tidal analysis package (Foreman 1978) to determine the tidal constituent magnitudes and phases (Fig. 4). The tidal constituents together accounted for nearly 95% of the total variance in the currents at each depth.

The M_2 harmonic is the largest in magnitude at all depths, followed by K_1. Below 40 m, the orientations of their tidal ellipses lie between east and 20° south of east. The slight depth variation in the tidal ellipses is believed to be caused by internal tides and by bottom friction (Ott 2000). The mean orientation of the M_2 and K_1 tidal ellipses below 50-m depth was 10° south of east. This is chosen as the along-channel direction, with u and v positive up-channel and toward Vancouver Island, respectively.

The mean of the residual (detided) along-channel current u over the 21-day deployment shows the expected estuarine shear (Fig. 5a); the time-mean outflow in the upper layer was 0.26 m s^{-1} at 40 m while the maximum time-mean inflow was 0.13 m s^{-1}. The mean current was zero at 85 m, the same depth as Labrecque et al. (1994) found at a similar distance from the coast between May and July in 1975. The mean residual cross-channel current v (toward 10° east of north) is fairly large throughout much of the water column, peaking at about -0.06 m s^{-1} (i.e., toward Washington State) at 95-m depth. The mean vertical current w reveals a 20-m-thick convergence layer centered (i.e., with maximum $|\partial w/\partial z|$) at 87 m, just above a 10-m-thick divergence layer centered at 100 m. The daily means of the along- and cross-channel velocities are shown in Figs. 5b and 5c , respectively.

The horizontal current components depend on the choice of axes. The along-channel current is essentially unchanged by small rotations of the (u, v) axes away from the mean inclination of the M_2 tidal ellipse, 10° south of east (Fig. 6a). The geostrophic along-channel flow, based on the stratification at several CTD stations on the C line and for a range of cross-channel surface pressure gradients p_y is also shown. The geostrophic current between the stations C6 and C8, those directly on either side of the ADCP, suggests that the surface pressure gradient is about 3×10^{-2} Pa m^{-1}. The fact that the measured current does not appear to be geostrophic over much of the water column suggests that the dynamics are sufficiently localized that the hydrography at the nearest CTD stations, which are more than 1500 m away, is not representative of the local mean hydrography, or that strong ageostrophic currents exist.

Cross-channel currents in the upper and lower layers are significantly altered under axis rotations of 5° (Fig. 6b), but the strong transverse currents at middepth are robust. The geostrophic cross-channel currents calculated from various along-channel CTD station pairs are remarkably similar, especially below 40-m depth. The along-channel pressure gradient just below the sea surface, determined by equating the measured and geostrophic currents at the top of the Ekman layer (105-m depth), is found to be $p_x \simeq 2 \times 10^{-3}$ Pa m^{-1}. This value is about one-half of the late-summer long-term mean for Juan de Fuca Strait obtained from tide gauges and atmospheric pressure measurements by Ott and Garrett (1998) and used in their momentum-balance calculation of the eddy viscosity parameter at interfacial depths. The smaller pressure gradient is largely offset by an increase in $\partial U/\partial z$ to about $-0.2/50$ s^{-1} between 60 and 100 m (Fig. 2), or about 50% larger than the value used in Ott and Garrett (1998), implying $A_v \approx 0.015$ m^2 s^{-1} in the interfacial region.

The increase in shear may be the result of either interannual variability or a lack of vertical resolution in the previous study (Ott and Garrett 1998). In that study, the subsurface pressure gradient was assumed to be zero in the winter; either this assumption is incorrect, or the situation in 1996 was significantly different from the long-term mean, or the along-channel sea-surface pressure gradient in the middle section of the strait is less than in the strait as a whole. Of interest, the results of the Masson and Cummins (1999) numerical model of the currents on the west coast of Vancouver Island and inside Juan de Fuca Strait show that most of the sea surface drop inside the channel occurs near the mouth; that is, the pressure gradient inside the strait may indeed be lower.

If the transverse flows are ageostrophic and result from internal friction, there should be evidence of instability and eddy momentum flux. We examine these issues next.

b. Shear instability

The strong shears in the along- and cross-channel directions suggest that the flow may be unstable to shear instabilities despite the strong stratification. We need to examine the Richardson number $Ri \equiv N^2/|\mathbf{u}_z|^2$ where $\mathbf{u}_z$ is the vertical shear in the ADCP current.

Variations in the density profiles are small over a tidal cycle (Fig. 3c ⊙) and also from day to day over the spring–neap cycle (Ott 2000). We therefore use $N(z)$ (Fig. 3f ⊙) from the overall mean stratification (Fig. 3e ⊙), with a resolution of 2 m to match that for the current shear. In evaluating the shear we could use data sampled at 30 s, but this rate may represent some instability itself rather than the background shear responsible for the instability. Moreover, the horizontal current estimate from the ADCP requires that the horizontal current be homogeneous over the beam separation, which is unlikely to be true at short timescales. To be sure, the contamination of the horizontal velocity by the weaker vertical component may be small, but overall it seems appropriate to present Richardson numbers based on a longer averaging time of the horizontal current. We choose 1 h, because this is longer than the typical buoyancy period of about 10 min but still much less than the tidal period.

Figure 7 ⊙ shows the 20 days of Richardson number estimates. Low values are common at depths below 110 m, which is not surprising given the strong tidal shear and weak stratification in the bottom well-mixed layer. At middepths, however, low Richardson numbers are much more common around the neap tides, centered on 24 July, than around the spring tides. There is no obvious relationship of the frequency of low Richardson numbers to the phase of the tide, illustrated here by the tidal current at 80 m, except, perhaps, for an indication on 24–28 July that lower Richardson numbers at middepth tend to occur on the transition from ebb to flood tide.

At middepths, maxima in the frequency with which the flow is potentially unstable to shear instability are found at 90 m, just below the interface between the inflow and outflow, where the 1/4 criterion (Miles 1961) is reached more than 60% of the time at neap tide and less than 10% of the time at spring tide (Fig. 8a ⊙). Between 85- and 95-m depth, the spring–neap difference in Richardson number is considerable (Fig. 8b ⊙). That is, Richardson numbers during spring tide are much larger than during neap tide. The spring–neap variation in the percentage of lower Richardson numbers between 80- and 90-m depth (Fig. 8c ⊙) also reveals that the current is most unstable during neap tide. The increase on 31 July (spring tide) is related to bottom shear; the incidence of low Richardson numbers decreases when averaging over regions higher in the water column and increases as the bottom is approached.

The low Richardson numbers discussed above are strong indications of the potential for flow instability. We turn next to results on the Reynolds stresses, which can be calculated directly from high-resolution ADCP data without requiring horizontal homogeneity.

c. Reynolds stress

To determine the Reynolds stresses $\overline{u'w'}$ and $\overline{v'w'}$, we first define the three-dimensional perturbation velocity (u', v', w') by detrending short sections, of between 10- and 80-min duration, of the total (tidal and residual) ADCP current data. The auto- and cross-correlations are calculated by averaging the products of the these perturbation velocities over the same time period. It can be shown (e.g., van Haren et al. 1994; Lu and Lueck 1999) that the $\overline{u'w'}_u$ and $\overline{v'w'}_v$ cross-correlations provide unbiased estimates of the Reynolds stress under the assumption of statistical homogeneity, provided that the (u, v) axes are aligned with the ADCP beam directions and that w_u is the vertical velocity calculated from beams 1 and 2 and w_v is calculated from beams 3 and 4. The above formulas are equivalent to the more conventional calculations using beam variances (e.g., Lohrmann et al. 1990). On the other hand, estimates of $\overline{u'u'}$ are biased by differences in w from beam to beam (Ott 2000). Given that w is typically much less than u, the bias in u', and hence in $\overline{u'u'}$, is likely to be fairly small. Moreover, $\overline{u'u'}$ is only used as a rough estimate to show that the measured $\overline{u'w'}$ is not a result of w' being contaminated by u'. The same argument applies to $\overline{v'v'}$ and $\overline{v'w'}$.

Interfacial Reynolds stresses after the neap tide are about an order of magnitude larger than after the spring tide (Fig. 9 ⊙). In addition, the variation with depth during spring tide is irregular; that during neap tide has definite vertical structure. Both these facts suggest that, although the signal during spring tide is likely noise, the larger Reynolds stresses during neap tide provide evidence of the shear instability anticipated from the low Richardson numbers. The stress magnitudes during neap tide are relatively independent of the choice of averaging time (between 10 and 80 min), suggesting that a spectral gap exists.

At the other end of the frequency spectrum, the key question is whether sampling only every 30 seconds—that is, in burst mode with 35 pings in 11 s in order to obtain a more robust estimate of the current—resulted in the loss of a significant part of the stress. We assume not, given that the timescale of the turbulence is likely to be on the order of π/N (e.g., Crawford 1986), which is 5 min in our case. Moreover, the cross-spectra between u and w typically fall off at high frequencies close to the Nyquist frequency.

A further issue is the 2-m vertical bin size relative to the expected scale of the overturning eddies. At times of large Reynolds stress (Figs. 10g,h,i ⊙), it seems that both u' and w' must be several times 10^{-2} m s^{-1}. A mixing-length interpretation of u' as lU_z would then give an estimate of about several meters for the mixing length l. As an alternative, an overturn scale might be on the order of w'/N, again several meters. The expected vertical scale of eddies is thus not much larger than the bin size, and it is possible that the Reynolds stress has been underestimated. The expected horizontal scale of the eddies is expected to be larger than the vertical scale because of the stratification, so the horizontal bin size is likely to be less of an issue.

Since the vertical velocity is the smallest component, it is most susceptible to errors, raising the fear that the Reynolds stresses we have found are artifacts. Ott (2000) examined several sources of error, including the effects of the diurnal zooplankton migration and of biases in the measured ADCP pitch and roll angles. He concluded that the vertical velocities, and in particular the estimates of w' used in estimating the Reynolds stress, are significantly different from zero. Moreover, during neap tide, peaks in $\overline{u'w'}$ at 70- and 95-m depths are about 20% of the corresponding values in $\overline{u'u'}$. Were the $\overline{u'w'}$ signal purely a result of horizontal fluctuations (u' or v') contaminating the vertical velocity w', the error in the measured pitch and roll angle would have to be of the order of 10° to account for the observed signals. Furthermore, with $\overline{u'u'}$ on 1 August at least 25% of the peak value on 25 July (Fig. 9c ⊙), such large pitch and roll biases would imply $\overline{u'w'} \approx 10^{-3}$ m^2 s^{-2} on 1 August, much larger than the values seen. The tilt errors required to account for the peaks in $\overline{v'w'}$ at 75-m depth are similar. In addition, the 95% confidence intervals, determined using the bootstrap technique (von Storch and Zwiers 1998) are small when compared with the magnitude of the cross correlations at neap tide. At spring tide, the results are not statistically different from zero.

We conclude that the measured cross correlations at neap are good estimates of the actual Reynolds stresses (per unit mass), despite some concern over the effect of the finite bin size, and that the spring–neap variation in the interfacial Reynolds stress is significant, as is the vertical variation in the sign of the Reynolds stress at neap tides. These are consistent with the reduced Richardson numbers found during neap tide (Fig. 8 ⊙), as well as with the enhanced estuarine exchange at this time.

Although the surface salinity at Race Rocks has largely recovered by 31 July from the anomalously low values over much of the previous month (Fig. 2 ⊙), indicating a return to a more common spring–neap cycle in the estuarine exchange, there is some indication that Reynolds stresses during the neap tide of 8 August are again significant, or growing. Thus, although it may be that the measured stresses we measured in July were enhanced as compared with the regular neap values, the data suggest that a regular spring–neap variation in the mixing in Juan de Fuca Strait exists.

To facilitate a comparison between the Reynolds stresses measured with the ADCP, the calculated Richardson numbers, and the spring–neap variation in the mean flow, $\overline{u'w'}$ (Fig. 10 ⊙) and $\overline{v'w'}$ (not shown) are rotated into along- and cross-channel directions. The strongest neap $\overline{u'w'}$ stresses occur between strong ebb and the following flood tides (Figs. 10g–j ⊙). This is true both below 85 m, where the stresses are predominantly negative, and above 85 m, where the stresses are positive. The stresses occur at the same depths and times as the low Richardson numbers (Figs. 7g–j ⊙).

With the exception of the bottom boundary layer, Reynolds stresses during spring tide are not significantly different from zero throughout the water column (Figs. 11a,b ⊙). The mean bottom stress acting on the water can be parameterized as $\tau/\rho = -4/\pi C_D U_T u$, where U_T is the magnitude of the tidal current and u is the mean near-bottom velocity. Ott (2000) used log-layer fitting of vertical profiles of the total current to calculate bottom drag coefficients of $C_D \approx 3 \times 10^{-3}$ for both ebb and flood tides at the ADCP site during the 21-day deployment. With $U_T \approx 1$ and 0.5 m s^{-1} at spring and neap tide, respectively, and $u \approx 0.1$ m s^{-1}, the Reynolds stress should be on the order of -4×10^{-4} m^2 s^{-2} at spring tide, and one-half of this value at neap tide. The measured value of the Reynolds stress near the bottom is in rough agreement, with $\overline{u'w'} \approx -2 \times 10^{-4}$ m^2 s^{-2}, and is about one-half that at neap tide (Fig. 11a ⊙). The variation of the large bottom Reynolds stress (i.e., in the lower two bins) with respect to the phase of the tide is also correct, as can clearly be seen by comparing Figs. 7 ⊙ and 10 ⊙. On the larger flood tides, when positive tidal velocities combine with the positive mean inflow at depth, the stresses are negative. During weak flood tides, stress magnitudes are less than 2×10^{-4} m^2 s^{-2}. On ebb tides, the mean estuarine inflow at depth offsets part of the ebb current, resulting in currents which are weaker in magnitude than those seen on flood. The bottom stress at these times is again smaller in magnitude than 2×10^{-4} m^2 s^{-2}. Further details are discussed by Ott (2000).

At middepths where the observed Reynolds stresses are significant, we wish to relate them to ageostrophic flows. One first step is to see if the stresses have a simple interpretation in terms of an eddy viscosity.

d. The vertical eddy viscosity

The enhanced estuarine exchange and transverse flows at neap tide (Figs. 12a,b ⊙) lead to larger total shears, particularly between 80- and 90-m depth. As a result, the gradient Richardson number is considerably smaller over these depths during neap tide (Fig. 8 ⊙). The vertical eddy viscosity, parameterized as $A_v \equiv -\overline{u'w'}/U_z$, with U_z the vertical shear in the 3-day mean along-channel velocity over 2 m is positive and increases with height above the bottom in the lowest 15 m, reaching approximately 0.10 m² s⁻¹ during neap tide and 0.15 m² s⁻¹ at spring tide (Fig. 12e ⊙). This is the expected result for wall-bounded flow, where eddy sizes are restricted close to the solid boundary (Ott 2000).

Above 80 m and between 100 and 120 m, the shear is weak, magnifying uncertainties in the measured Reynolds stress so that the vertical eddy viscosity parameter A_v is not statistically significant (Fig. 12e ⊙). In the interfacial region (between 80 and 100 m), however, A_v is significant. It varies with depth and is positive above and negative below the interface. Above the interface (at 80 m), the A_v averaged over the neap tides is on the order of 0.1 m² s⁻¹. This is consistent with an estimate from the limited microstructure data where $A_v = \epsilon/U_z^2 \simeq 0.05$ m² s⁻¹. Masson and Cummins (2000, personal communication) estimate a localized peak in the vertical eddy viscosity in central Juan de Fuca from a turbulence closure model of the flow (Masson and Cummins 2000), with a peak value of $A_v \simeq 0.02$ m² s⁻¹. Ott and Garrett (1998) indicate a mean value of 0.02 m² s⁻¹ is necessary to satisfy an along-channel momentum balance. However, the observed sign change across the interface is inconsistent with a simple scenario in which local shear instability of the mean flow acts to smooth the mean velocity profile. We return later to other possibilities, but remark for now that, regardless of the sign of any eddy viscosity, the divergence of the Reynolds stress may still be compared with low-frequency ageostrophic motions.

e. Effect of mixing on the mean flow

The vertical divergence of the Reynolds stresses appears explicitly (without any requirement of parameterization) in the slowly varying horizontal momentum equations

$$\partial u/\partial t + \mathbf{u} \cdot \nabla u + (\overline{u'w'})_z - fv_a = 0, \quad \text{and} \quad (2)$$

$$\partial v/\partial t + \mathbf{u} \cdot \nabla v + (\overline{v'w'})_z + fu_a = 0, \quad (3)$$

where $(u_a, v_a) \equiv (u - u_g, v - v_g)$ is the horizontal ageostrophic velocity and (u_g, v_g) is the slowly varying geostrophic velocity from the pressure gradient. In the advective term, $\mathbf{u}$ is the three-dimensional velocity (u, v, w). As discussed by Gill (1982), small ageostrophic flows are associated with the slow changes in a quasigeostrophic flow. They are also induced, however, by divergence of the Reynolds stresses.

We first examine the terms in (3). We have already found that there appears to be a significant imbalance between the 21-day along-strait average current and the geostrophic flow implied by a cross-strait hydrographic survey (Fig. 6a ⊙). The unknown value of the cross-strait near-surface pressure gradient means that we do not know the precise value of the discrepancy, but it may be about 0.1 m s⁻¹, giving $fu_a = O(10^{-5})$ m s⁻². This is much larger than any possible value of $\partial v/\partial t$ for that period, though the magnitude of the advective terms is unknown. The 21-day average of the Reynolds stress divergence in (3), based on taking the values in Fig. 11 ⊙ for about 20% of the record and zero for the rest of the time, may also be $O(10^{-5})$ m s⁻², but without any matching vertical structure. It thus does not seem possible to ascribe the apparent presence of a 21-day ageostrophic along-strait current u_a to the action of Reynolds stresses; it seems more likely to be a consequence of our limited hydrographic survey. Uncertainty in the changing hydrography also prevents any useful deduction from (3) treated as an equation for the slowly varying flow.

We turn next to (2). Here the vertical structure of the apparent ageostrophic cross-strait flow v_a (Fig. 6 ⊙) seems unlikely to have been associated with uncertainties in the along-strait density structure. Moreover, the cross-strait flow was strongest during the period from 24 to 26 July when the Reynolds stresses were significant. Given this time dependence, we need to establish the relative importance of $\partial u_a/\partial t$ and fv_a in balancing the forcing term in (2). A simple intuition-building example would be with constant geostrophic flows, so that $(\partial u/\partial t, \partial v/\partial t) = (\partial u_a/\partial t, \partial v_a/\partial t)$, with the forcing Reynolds stress term $-\overline{u'w'}_z$ in (2) equal to $F \cos\omega t$, and with no Reynolds stress term in (3). The response is

For slow changes in the forcing, so that ω/f is small, the ageostrophic response is close to the steady response $(u_a, v_a) = (0, -F/f)$. The effect on v of a slowly varying forcing term in (3) will similarly be small. If the changes were gradual over the spring–neap cycle, then ω/f would be about 0.05. In fact, the changes we find seem to be more rapid near neap tide, with a value of ω/f of more like 0.1 if we fit one-half of a period of 4 days to the changes in Reynolds stress shown in Fig. 9a ⊝, but we still expect the primary response to be an ageostrophic cross-strait flow given by $v_a \simeq \overline{(u'w')}_z/f$ if the advective terms can be ignored.

Contours of the daily means of the nonadvective terms in (2) reveal that the acceleration term is an order of magnitude smaller than either the Reynolds stress forcing term or the cross-channel ageostrophic velocity (Fig. 13 ⊝). The latter two have some similarity, although increases in v_a at neap tide (1 August) are not associated with elevated Reynolds stress levels. This mismatch is perhaps to be expected in the presence of along-strait inhomogeneity; the local ageostrophic v_a is likely to be a consequence of upstream forcing that may differ from the local Reynolds stress divergence, and local forcing will manifest itself elsewhere.

Another possibility is that the tidal stresses $\langle \partial u_T u_T/\partial x \rangle$, $\langle \partial u_T v_T/\partial y \rangle$, and $\langle \partial u_T w_T/\partial z \rangle$ (where $\langle\ \rangle$ denote tidal average) are important in (2). Using a scaling argument with along- and cross-channel length scales of $(L_x, L_y) \approx (100, 10)$ km and overestimates for the tidal flow of $(u, v) \approx (1, 0.1)$ m s^{-1}, the first and second of these tidal stress terms are at most 10^{-5} m s^{-2}, an order of magnitude smaller than the values of $\overline{(u'w')}_z$ measured. The final term, $\langle u_T w_T \rangle_z$, can be determined from the tidal constituents of the ADCP data. The tidally averaged stresses at all depths are less than 10^{-4} m s^{-2} for all tidal constituents except M_2, for which values approach 2×10^{-4} m s^{-2} at 105 m and -2×10^{-4} m s^{-2} at 90 m. Nevertheless, the M_2 stress remains constant throughout the deployment, whereas both the Reynolds stress and the cross-channel currents increase at neap tides. In the cross-channel momentum balance, $\langle u_T v_T \rangle_x$ and $\langle v_T v_T \rangle_y$ are, from scaling arguments, at most 10^{-6} m s^{-2}, whereas $\langle v_T w_T \rangle_z$ is less than 2×10^{-5} m s^{-2} at all depths and for all constituents.

f. Microstructure

The occurrence of turbulent mixing near the interface between the deep inflow and the surface outflow is also evident in the limited microstructure profile data. Seventeen microstructure profiles were collected over a 2-h period spanning the slack tide at noon on 5 August 1996 (Fig. 14 ⊝), corresponding to neap tides. The tide was changing from a flood (dominant inflow at depth) to an ebb (dominant outflow at the surface). During the slack tide, elevated dissipation rates were measured between 60- and 100-m depth, with peak values on the order of $\epsilon = 3 \times 10^{-5}$ W kg^{-1}. No significant dissipation rates were recorded elsewhere, either spatially or temporally.

The dissipation could arise from the divergence of the energy flux of internal waves, and could occur without a mean shear. Internal wave interactions with the mean shear could also produce local turbulence. An examination of the production of turbulence by $-\overline{u'w'}U_z$ from the ADCP data on 5 August reveals significant production between 0900 and 1100 LT at 80-m depth, over an hour before the elevated dissipation rate measurements were observed by microstructure profiling. Direct coincidence in both space and time for the production and dissipation of turbulence, however, may not be necessary in such an advective environment. Suffice it to say that these independent observations both indicate periods of strong turbulence near the exchange flow interface.

5. Summary and discussion

We have been able to obtain reliable estimates of Reynolds stresses in a stratified shear flow away from boundaries. Large stresses occur at neap tide and seem to be associated with times of reduced Richardson number. The fortnightly variation in this stress provides more confidence in the measurements and is also interesting in its own right. The variation is consistent with greater mean shear at neap tide due to the enhanced estuarine exchange which is, in turn, controlled upstream by the spring–neap cycle in the vertical transport of momentum in the San Juan and Gulf Islands.

The stress itself does not seem to be simply related to the local shear in terms of a positive eddy viscosity, with both positive- and negative-stress regions bounding the high-shear interface. This finding casts doubt on the parameterizations used in some numerical models, although the magnitudes of the localized eddy viscosities are comparable. The actual cause of the Reynolds stress is uncertain. Critical layer absorption of internal waves seems unlikely because it would require constant $\overline{u'w'}$ below the critical level and very small values above, which are not supported by the measurements. It may be

that flow instabilities are triggered by the interaction of internal wave shear and mean flow shear.

There is some qualitative agreement between the Reynolds stress divergence and the ageostrophic cross-strait flow, though no precise quantitative correspondence. This disagreement could be associated with spatial inhomogeneity in the forcing and response so that the advective terms are also important in the equations of motion.

Given the inhomogeneity of the natural world, it is difficult to measure everything everywhere. The key challenge must be to focus on observations which allow verification, or invalidation, of proposed parameterization schemes. To that end, additional measurements of the Reynolds stress, as well as of the background fields entering the parameterization scheme, are required.

On a local scale, an interesting issue is the effect of freshwater pulses on the spring–neap cycle in the estuarine exchange and on mixing within the strait. Northwesterly winds in the Strait of Georgia during neap tides result in an additional increase in the exchange flow on occasion, and surface salinity data from Race Rocks suggest that such an event occurred over the time of the ADCP deployment. Preliminary analysis from an ADCP deployment in the summer of 1998, at which time sea surface salinities at Race Rocks were not reduced, reveals that mean currents at neap tide were not enhanced as much as was found in 1996.

REFERENCES

Crawford W. R., 1986: A comparison of length scales and decay times of turbulence in stably stratified flows. *J. Phys. Oceanogr.*, **16**, 1847–1854. Find this article online

Csanady G. T., 1972: Secondary circulation near an upwelled interface. *Proc. Canadian Committee on Oceanography Conf.,* Burlington, ON, Canada, 41.

Dewey R. K., and W. R. Crawford, 1988: Bottom stress estimates from vertical dissipation profiles on the continental shelf. *J. Phys. Oceanogr.*, **18**, 1167–1177. Find this article online

Dewey R. K., W. R. Crawford, A. E. Gargett, and N. S. Oakey, 1987: A microstructure instrument for profiling oceanic turbulence in coastal bottom boundary layers. *J. Atmos. Oceanic Technol.*, **4**, 288–297. Find this article online

Fischer H. B., E. J. List, R. C. Y. Koh, J. Imberger, and N. H. Brooks, 1979: *Mixing in Inland and Coastal Waters*. Academic Press, 483 pp.

Foreman M., 1978: Manual for tidal currents analysis and prediction. Pacific Marine Science Rep. 78-6, 57 pp.

Gill A. E., 1982: *Atmosphere–Ocean Dynamics*. Academic Press, 662 pp.

Griffin D., and P. LeBlond, 1990: Estuary/ocean exchange controlled by spring–neap tidal mixing. *Estuarine Coastal Shelf Sci.*, **30**, 275–297. Find this article online

Hansen D., and M. Rattray, 1966: New dimensions in estuary classification. *Limnol. Oceanogr.*, **11**, 319–326. Find this article online

Johnson G. C., and T. B. Sanford, 1992: Secondary circulation in the Faroe Bank Channel outflow. *J. Phys. Oceanogr.*, **22**, 927–933. Find this article online

Johnson G. C., and D. R. Ohlsen, 1994: Frictionally modified rotating hydraulic channel exchange and ocean outflows. *J. Phys. Oceanogr.*, **24**, 66–78. Find this article online

Labrecque A. J. M., R. E. Thomson, M. W. Stacey, and J. R. Buckley, 1994: Residual currents in Juan de Fuca Strait. *Atmos.–Ocean*, **32**, 375–394. Find this article online

Lohrmann A., B. Hackett, and L. P. Roed, 1990: High resolution measurements of turbulence, velocity and stress using a pulse-to-pulse coherent sonar. *J. Atmos. Oceanic Technol.*, **7**, 19–37. Find this article online

Lu Y., and R. G. Lueck, 1999: Using a broadband ADCP in a tidal channel. Part II: Turbulence. *J. Atmos. Oceanic Technol.*, **16**, 1568–1579. Find this article online

MacCready P., 1999: Estuarine adjustment to changes in river flow and tidal mixing. *J. Phys. Oceanogr.*, **29**, 708–726. Find this article online

Masson D., and P. F. Cummins, 1999: Numerical simulations of a buoyancy-driven coastal countercurrent off Vancouver Island. *J. Phys. Oceanogr.*, **29**, 418–435. Find this article online

Masson D., and P. F. Cummins, 2000: Fortnightly modulation of the estuarine circulation in Juan de Fuca Strait. *J. Mar. Res.*, **58**, 439–463. Find this article online

Mertz G., and Y. Gratton, 1995: The generation of transverse flows by internal friction in the St. Lawrence estuary. *Cont. Shelf Res.*, **15**, 789–801. Find this article online

Miles J. W., 1961: On the stability of heterogeneous shear flows. *J. Fluid Mech.*, **10**, 496–508. Find this article online

Ott M. W., 2000: Mixing and secondary circulation in Juan de Fuca Strait. Ph.D. thesis, University of Victoria, 162 pp.

Ott M. W., and C. Garrett, 1998: Frictional estuarine flow in Juan de Fuca Strait, with implications for secondary circulation. *J. Geophys. Res.*, **103**, 15657–15666. Find this article online

Rattray M. Jr.,, and D. V. Hansen, 1962: A similarity solution for circulation in an estuary. *J. Mar. Res.*, **20**, 121–133. Find this article online

Stacey M. T., S. G. Monismith, and J. R. Burau, 1999a: Measurement of Reynolds stress profiles in unstratified tidal flow. *J. Geophys. Res.*, **104**, 10933–10949. Find this article online

Stacey M. T., S. G. Monismith, and J. R. Burau, 1999b: Observations of turbulence in a partially stratified estuary. *J. Phys. Oceanogr.*, **29**, 1950–1970. Find this article online

van Haren H., N. Oakey, and C. Garrett, 1994: Measurements of internal wave band eddy fluxes above a sloping bottom. *J. Mar. Res.*, **52**, 909–946. Find this article online

von Storch H., and F. Zwiers, 1998: *Statistical Analysis in Climate Research*. Cambridge University Press, 484 pp.

Figures
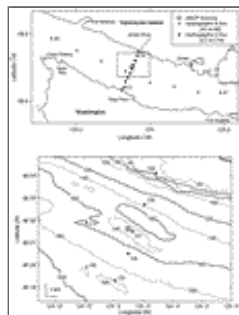
Click on thumbnail for full-sized image.

FIG. 1. (top) 1996 CTD and ADCP mooring locations in Juan de Fuca Strait and (bottom) a detailed region near the ADCP mooring showing the bathymetry in meters

Click on thumbnail for full-sized image.

FIG. 2. Daily surface salinity recorded at Race Rocks for 1996. The thick line indicates the deployment period, and the triangles denote neap tide
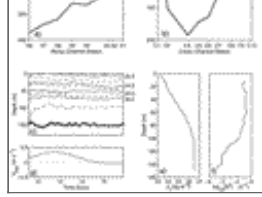
FIG. 3. Contours of σ_t for (a) an along-channel transect, (b) a cross-channel transect, and (c) the time series taken at the ADCP station. The contour interval is 0.5 kg m^{-3}, with the numbers to the right of each plot corresponding to the solid lines. The bottom is indicated by the thick line. Plus marks in (c) indicate individual profiles in the time series. (d) The tide (positive to the east) at 80-m depth. (e) The mean density profile over the deployment. (f) The corresponding buoyancy frequency
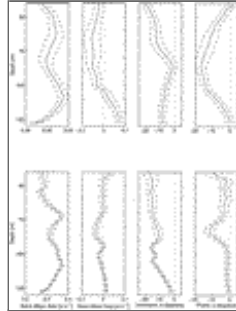
FIG. 4. Tidal parameters for the (top) M_2 and (bottom) K_1 tidal constituents, with dashed lines indicating the 95% confidence intervals. An inclination of 0° is eastward. The phase is relative to that of the tide in the lowest bin
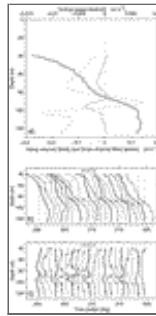
FIG. 5. Mean residual (i.e., detided) currents in Juan de Fuca Strait: (a) over the entire deployment, (b) daily along-channel means, and (c) daily cross-channel means. The (x, y) axes are rotated 10° clockwise from (east, north). In (b) and (c), plus signs indicate zero velocities, and the ±0.1 m s^{-1} scale is shown at the top
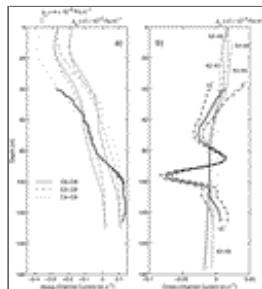
FIG. 6. Variation of measured (a) along-channel and (b) cross-channel current (thick) with axes rotation (degrees clockwise from east–north): 10 (solid), 15 (dash), and 5 (dot–dash). Also shown are the geostrophic velocities (thin), based on the hydrography at various pairs of CTD stations using the surface pressure gradients shown. The along-strait surface pressure gradient used, p_x $= 2 \times 10^{-3}$, is that for which the cross-channel geostrophic and measured currents match at the top of the Ekman layer (105 m)
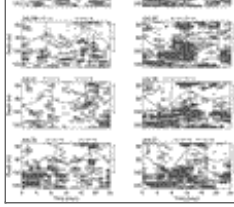
FIG. 7. Shear instability throughout the deployment as determined from the gradient Richardson number based on 1-h mean currents and the average stratification at the ADCP site. Dark and light regions indicate depths and times for which the Richardson number fell below 0.25 and 1, respectively. The solid horizontal profile is the along-channel tidal velocity at 80-m depth, with the ± 1 m s^{-1} scale plotted on the right. The vertical profiles are the hourly average total (i.e., tidal and residual) along-channel currents with the ± 1 m s^{-1} scales plotted above
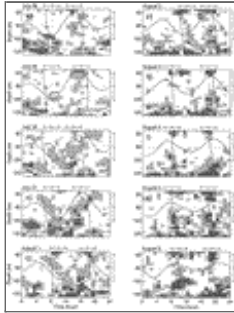
FIG. 7. (*Continued*)
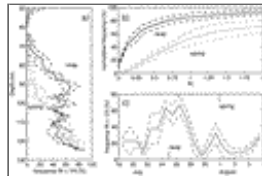
FIG. 8. Variation with depth and over the spring–neap cycle of the frequency (%) with which the gradient Richardson number, defined over 2 m, falls below 0.25. (a) Thick and thin lines indicate the period just after neap tide (24–26 Jul) and spring tide (31 Jul–2 Aug), respectively. The solid lines are 3-day averages and the dashed lines indicate the mean $\pm$ the standard deviation of the means for each day. (b) The mean cumulative frequency (%) for the depths between 80 and 90 m over days 206–208 and 213–215 are denoted by thick and thin lines, respectively. The dashed lines again indicate the mean $\pm$ the standard deviation over the 3 days and six depth bins. (c) The mean daily frequency with which Ri < 1/4 over the depth range 80–90 m (solid) and the mean $\pm$ the standard deviation of the means at each depth (dash)
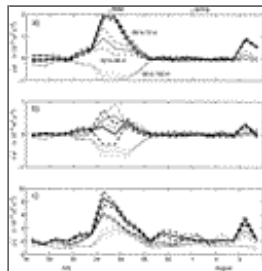
FIG. 9. Variation of (a) $\overline{u'w'}$ and (b) $\overline{v'w'}$ Reynolds stress as well as (c) $\overline{u'u'}$ throughout the spring–neap cycle. In each case, the solid lines represent the daily averages over the depth ranges shown and the dashed lines indicate the 95% confidence level calculated via the bootstrap technique. For (a) and (b), the (u, v) axes are rotated such that u is positive up-channel
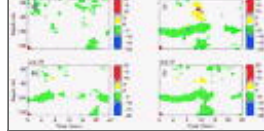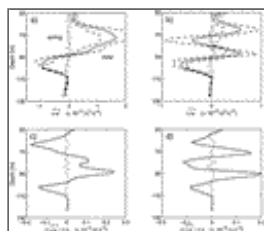
FIG. 10. Reynolds stress ($\overline{u'w'}$, 10^{-4} m^2 s^{-2}) throughout the deployment. Stresses of magnitude less than 2×10^{-4} m^2 s^{-2} are not shown
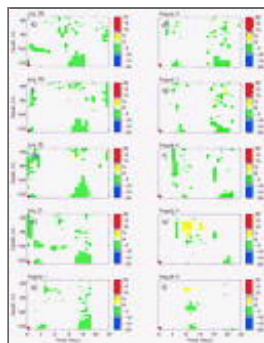
FIG. 10. (*Continued*)
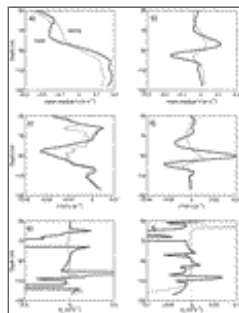
FIG. 11. Mean vertical Reynolds stress and vertical derivative over 3 days at neap (24–26 Jul, thick lines) and spring tide (31 Jul–2 Aug, thin lines). The dashed lines indicate the 95% confidence interval, calculated via the bootstrap technique

FIG. 12. Mean residual (a) along-channel and (b) cross-channel current with (c) and (d) associated shears. (e) (f) The corresponding parameterized vertical eddy viscosities. Thick lines are the 3-day averages at neap tide (24–26 Jul), thin lines during spring tide (31 Jul–2 Aug)
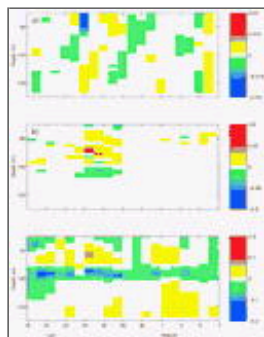
FIG. 13. Daily means of the nonadvective terms in (2) (m s^{-1}): (a) u_t/f, the acceleration of the total along-channel velocity divided by the Coriolis parameter; (b) $\overline{u'w'}/f$, the Reynolds stress divided by the Coriolis parameter; and (c) v_a, the ageostrophic cross-channel velocity
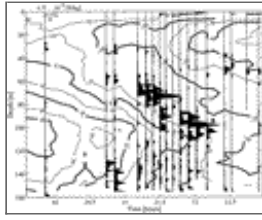
Click on thumbnail for full-sized image.

FIG. 14. Microstructure dissipation profiles on 5 Aug 1996, during the transition from flood to ebb. Dissipation rates are plotted on the linear scale shown in the upper-left corner. Contours denotes the along-channel current (cm s^{-1}).

* Current affiliation: College of Oceanic and Atmospheric Sciences, Oregon State University, Corvallis, Oregon

Corresponding author address: Michael W. Ott, College of Oceanic and Atmospheric Sciences, Oregon State University, Corvallis, OR 97333-5503. E-mail: mwott@coas.oregonstate.edu

top ▲